NRC Publications Archive
Archives des publications du CNRC

Deposition, microstructure and hardness of AlCoCrFeNi$_{2.1}$ eutectic high entropy alloy coatings by cold spray, HVOF, and plasma spray

Wei, Jingjie; Cojocaru, Cristian; Aghasibeig, Maniya; Shao, Chenwei; Li, Zehua; Zhang, Jiahui; Irissou, Eric; Zou, Yu

This publication could be one of several versions: author’s original, accepted manuscript or the publisher’s version. / La version de cette publication peut être l’une des suivantes : la version prépublication de l’auteur, la version acceptée du manuscrit ou la version de l’éditeur.

For the publisher’s version, please access the DOI link below./ Pour consulter la version de l’éditeur, utilisez le lien DOI ci-dessous.

Publisher’s version / Version de l'éditeur:

https://doi.org/10.1016/j.surfcoat.2024.131442

Surface and Coatings Technology, 494, P2, pp. 1-12, 2024-10-09

NRC Publications Archive Record / Notice des Archives des publications du CNRC :

https://nrc-publications.canada.ca/eng/view/object/?id=a858f733-39be-46a1-9619-3cbf3f6fdd94
https://publications-cnrc.canada.ca/fra/voir/objet/?id=a858f733-39be-46a1-9619-3cbf3f6fdd94

Access and use of this website and the material on it are subject to the Terms and Conditions set forth at https://nrc-publications.canada.ca/eng/copyright
READ THESE TERMS AND CONDITIONS CAREFULLY BEFORE USING THIS WEBSITE.

L’accès à ce site Web et l’utilisation de son contenu sont assujettis aux conditions présentées dans le site https://publications-cnrc.canada.ca/fra/droits
LISEZ CES CONDITIONS ATTENTIVEMENT AVANT D’UTILISER CE SITE WEB.

Questions? Contact the NRC Publications Archive team at PublicationsArchive-ArchivesPublications@nrc-cnrc.gc.ca. If you wish to email the authors directly, please see the first page of the publication for their contact information.

Vous avez des questions? Nous pouvons vous aider. Pour communiquer directement avec un auteur, consultez la première page de la revue dans laquelle son article a été publié afin de trouver ses coordonnées. Si vous n’arrivez pas à les repérer, communiquez avec nous à PublicationsArchive-ArchivesPublications@nrc-cnrc.gc.ca.

National Research Council Canada
Conseil national de recherches Canada

Surface & Coatings Technology 494 (2024) 131442

Contents lists available at ScienceDirect

Surface & Coatings Technology

journal homepage: www.elsevier.com/locate/surfcoat

Deposition, microstructure and hardness of $AlCoCrFeNi_{2.1}$ eutectic high entropy alloy coatings by cold spray, HVOF, and plasma spray

Jingjie Wei [a], Cristian Cojocaru [b], Maniya Aghasibeig [b], Chenwei Shao [a], Zehua Li [a], Jiahui Zhang [a], Eric Irissou [b], Yu Zou [a,*]

[a] Department of Materials Science and Engineering, University of Toronto, Toronto, ON M5S 3E4, Canada
[b] National Research Council Canada, Boucherville, QC J4B 6Y4, Canada

ARTICLE INFO

Keywords:
Cold spray
HVOF
Plasma spray
High entropy alloy
Microstructure

ABSTRACT

Eutectic high entropy alloys (EHEAs) are reported to exhibit excellent mechanical properties which are useful for coating applications. In this study, we have produced $AlCoCrFeNi_{2.1}$ EHEA coatings using the cold spray, high velocity oxygen-fuel (HVOF), and plasma spray techniques and compared their bonding characteristics, microstructure and hardness. We observe body-centered cubic (bcc) to face-centered cubic (fcc) phase transformations in all the types of coatings. The high processing temperatures in HVOF and plasma sprays lead to the segregation and depletion of Al from Ni-and Al-rich bcc/B2 regions and form Al_2O_3. In the cold sprayed coatings, we observe that a fraction of lamellar microstructure is preserved after cold spraying. Regarding the hardness, the cold sprayed coatings exhibit hardness in the range of 440–498 HV due to high work hardening and low oxygen content below 4 at.%; the HVOF coatings show the hardness in the range of 380–556 HV due to the effects of oxide dispersion strengthening with 13–28 at.% oxygen; The plasma sprayed coatings exhibit the hardness in the range 208–258 HV and 6.1–13.4 at.% oxygen. This study demonstrates the feasibility to produce thick and dense EHEA coatings using the above spray techniques, and the cold sprayed coatings exhibit relatively high hardness and low oxygen levels.

1. Introduction

High entropy alloys (HEA) are typically formed by mixing five or more principal elements of near equiatomic compositions to create a unique and stable solid solution with a high entropy of mixing [1–5]. Many of the HEAs exhibit excellent thermal stability, high temperature structural performance, corrosion and oxidation resistance [1–7]. Unlike the traditional single-phase solid-solution HEAs, $AlCoCrFeNi_{2.1}$ is a eutectic HEA (EHEA) consisting of both the face center cubic (fcc) and body center cubic (bcc/B2) phases arranged in lamellar microstructure [8–11]. While the eutectic lamellar structure brings great enhancement in the mechanical properties by attaining a combination of high strength and high ductility [8–11], it is crucial to ensure the precise control and preservation of composition and microstructure during the processing of the material. Conventional processing techniques which utilize high thermal input, such as casting, often have difficulty in ensuring the compositional homogeneity of the HEA as the material goes through melting and solidification [9]. Besides, high temperature processing may introduce undesired changes to the microstructure such as oxidation, elemental segregation, and grain coarsening [12,13].

Taking on a different path from the thermal input-based processing approaches, cold spray is a solid-state coating deposition technique known for its ability in preserving the composition and chemical homogeneity in the processed material [12,14–18]. Using a stream of supersonic propulsive inert gas in temperature well below the melting point of the processed material, the feedstock powder is projected towards a substrate [12]. The high kinetic energy of the particles at impact allows them to achieve severe plastic deformation at incredible strain rates, leading to successful particle bonding and interlocking [12,13,18]. During the entire process, the feedstock material is kept in its solid state, thus thermally induced defects such as elemental segregation and oxidation can be effectively mitigated [12,16]. As such, cold spray is a good candidate technique for the processing of EHEAs such as $AlCoCrFeNi_{2.1}$.

High velocity oxygen-fuel (HVOF) and plasma spray are two coating deposition techniques from the thermal spray family [17]. In HVOF, the

---

* Corresponding author.
E-mail address: mse.zou@utoronto.ca (Y. Zou).

https://doi.org/10.1016/j.surfcoat.2024.131442
Received 21 September 2024; Received in revised form 3 October 2024; Accepted 6 October 2024

Table 1

Elemental compositions of the $AlCoCrFeNi_{2.1}$ feedstock powder, measured values obtained from EDS Analysis.

	Composition (at.%)				
	Al	Co	Cr	Fe	Ni
Nominal	16.4	16.4	16.4	16.4	34.4
Measured	15.9	16.8	16.0	16.5	34.8

mixture of oxygen gas and a fuel, such as propane, kerosene, or hydrogen, is combusted in a chamber and accelerated to a focused stream of high velocity gas jet [17,19]. The temperature of the gas jet is high enough to partially or completely melt the feedstock particles as they are deposited onto the substrate [17,19]. In plasma spray, a high-pressure gas plasma torch is used to fully melt the feedstock particles into droplets, then accelerate them in a stream of high velocity gas towards the substrate [17,19]. Contrary to cold spray, both HVOF and plasma spray rely on the traditional thermal spray approach to melt the feedstock powder with high thermal energy. For example, dense $AlCoCrFeNi_{2.1}$ coatings were successfully produced by plasma spray [8].

Despite the continuous effort in the study of HEAs, the areas of applications for HEAs are still limited. Currently, MCrAlY materials are commonly used in the application of high-temperature protective coatings due to their thermal stability, high oxidation and corrosion resistance [20–22] In this study, the microstructure and mechanical properties of $AlCoCrFeNi_{2.1}$ coating produced by cold spray, HVOF, and plasma spray are evaluated and compared to understand the influence of different deposition process characteristics and parameters. There is a potential to explore the possibility of finding alternative HEA materials and processing techniques to the MCrAlY alloys in high temperature protective coating applications. We observe and correlate changes to the eutectic lamellar microstructure to the processing conditions, as well as signs of phase transformation and the mechanism driving them.

2. Materials and methods

2.1. Materials and coating deposition

In this study, a gas atomized feedstock powder of $AlCoCrFeNi_{2.1}$ (Heeger Materials, USA) with powder particle diameter up to 28 μm was used to deposit the coatings by cold spray (PCS-100, Plasma Giken, Japan), HVOF (JP5000, Praxair, USA), and plasma spray (Axial III Plus, Northwest Mettech, Canada). Table 1 shows the nominal and measured elemental compositions of the powder obtained from the supplier and by EDS cross-sectional analysis, respectively. The two sets of values are in close agreement with each other.

The processing parameters used for the three deposition techniques are listed in Table 2. CS and PS stand for cold spray and plasma spray, respectively. The substrate material was Inconel 625 Ni-based superalloy, and the propelling gas used in cold spray was nitrogen. The plasma spray coatings were sprayed with the carousel rotation of 76 RPM. For cold spray, the traverse speed of the spray gun was varied while the rest of the parameters were maintained the same. On the other hand, by varying parameters such as the stand-off distance (SOD) and the flow of the fuel mixture (kerosene, O_2, H_2), the processing temperature of the HVOF and plasma spray were varied. The optimal SOD in the HVOF coatings allows the particles to achieve maximum velocity while absorbing sufficient heat from the exposure to the high temperature jet stream [23]. When the SOD is too large, the particles may decelerate and cool down along with the jet stream prior to impact and bonding, thereby decreasing the effective processing temperature experienced by the particles.

2.2. Coating characterization

The cross-sections of the feedstock powder and coatings were examined using a scanning electron microscope (SEM, JEOL JSM-6610LV, Tokyo, Japan). From the SEM micrographs, the average porosity and particle aspect ratio of the coatings were measured by image processing software ImageJ. The particle aspect ratio is the ratio of the longest axis to shortest axis of the deposited particles in the coatings, and 100 randomly selected particles from each coating were measured. Energy dispersive spectroscopy (EDS, X-Max, Oxford Instruments Ltd., UK) was conducted to analyze the elemental composition and distribution of the coating cross-sections. To capture the elemental composition of the fine lamellar structure, electron probe microanalyzer (EPMA, JOEL JXA-8230, Tokyo, Japan) was used to conduct wavelength dispersive X-ray spectroscopy (WDS) mapping on the cross-sections of the powder, CS 1, HVOF 1, and PS 3 coatings. X-ray diffraction (XRD, Philips PW1830) was conducted for the feedstock powder and the coatings with a 2θ scan step size of 0.05° and a scan time of 2.5 s per step using a Cu Kα source. To evaluate the hardness of the coatings, microindentation hardness tester (LECO, LM310AT, MI, USA) was used to perform Vickers microindentaion testing on both polished top and cross-sectional surfaces of the coatings. Ten measurements were taken with a load of 300 g and a dwell time of 10 s.

3. Results

3.1. Microstructure and properties of feedstock powder particles

Fig. 1 illustrates a set of characterization results of the gas atomized $AlCoCrFeNi_{2.1}$ powder. The spherical morphology of the powder is shown in Fig. 1-a. A logit scale was used to present the particle size distribution (PSD) of the powder to show the significant amount of fine size satellite particles which can also be observed in Fig. 1-a. Back-scattered electron (BSE) micrograph of the polished powder cross-section and results of the WDS elemental mapping are shown in Fig. 1-b and c, respectively. From the BSE micrograph, regions with darker contrast indicate a lower signal density, suggesting that the average atomic number of the local region (NiAl-rich) is smaller as compared to regions with brighter contrast (FeCoCr-rich). The lamellar

Table 2

Processing parameters used in the cold spray (CS), HVOF, and plasma spray (PS).

Coating	Parameter								
	Pgas (MPa)	Tgas (°C)	SOD (mm)	Vgun (mm/s)	Kerosene (lph)	O_2 (lpm)	Ar (lpm)	N_2 (lpm)	H_2 (lpm)
CS 1	7.5	950	50	50	–	–	–	–	–
CS 2	7.5	950	50	100	–	–	–	–	–
CS 3	7.5	950	50	200	–	–	–	–	–
HVOF 1	–	–	305	635	20	800	–	–	–
HVOF 2	–	–	203	635	20	800	–	–	–
HVOF 3	–	–	305	635	27	1030	–	–	–
HVOF 4	–	–	203	635	27	1030	–	–	–
PS 1	–	–	75	5	–	–	225	12.5	12.5
PS 2	–	–	75	5	–	–	175	50	25
PS 3	–	–	75	5	–	–	125	75	50

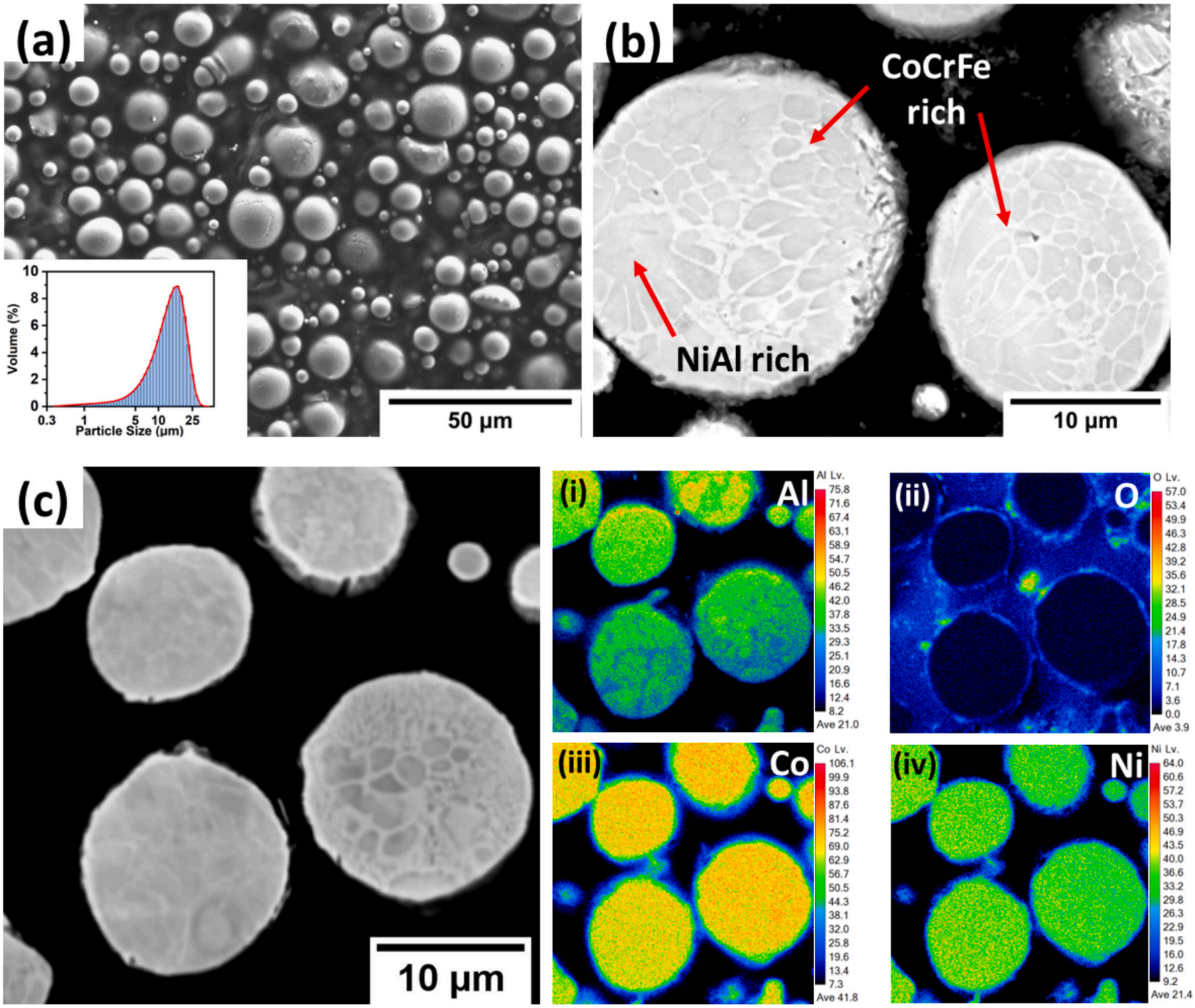

Fig. 1. (a) Powder particle morphology of the $AlCoCrFeNi_{2.1}$ feedstock, with the particle size distribution in logit scale at the lower left, (b) SEM micrograph of powder cross-section showing the lamellar structure with the NiAl-rich bcc/B2 region and CoCrFe-rich fcc region highlighted by the red arrows, and (c) WDS elemental mapping of the powder cross-section for (i) Al, (ii) O, (iii) Co, and (iv) Ni. The NiAl-rich bcc region is observed from the distribution of Al.

Table 3
Measured average porosity and particle aspect ratio of the sprayed coatings.

	CS 1	CS 2	CS 3	HVOF 1	HVOF 2	HVOF 3	HVOF 4	PS 1	PS 2	PS 3
Porosity (%)	1.52 ± 0.89	1.90 ± 0.90	2.12 ± 0.37	0.94 ± 0.16	0.21 ± 0.04	0.20 ± 0.03	0.09 ± 0.04	1.64 ± 0.40	0.17 ± 0.07	0.84 ± 0.18
Particle aspect ratio	2.57 ± 0.77	2.45 ± 0.77	2.16 ± 0.54	1.94 ± 0.75	–	–	–	1.37 ± 0.38	–	–

structure can be clearly observed: The FeCoCr-rich fcc region appears as the thin submicron layers that wraps and embeds the NiAl rich bcc/B2 regions. The feature size of the lamellar structure is in the sub-microscale region. The distribution of Al well separates the two phases and defines the bcc/B2 regions. Oxygen was only detected in the epoxy mount and the very thin outer layers of the powder particles, indicating that the powder does not suffer noticeable contamination from oxidation.

3.2. *Coating porosity and particle aspect ratio*

The porosity and particle aspect ratios of the coatings are measured, as shown in Table 3. Overall, the cold sprayed coatings show the highest porosity, contrary to the low porosities achieved in the HVOF coatings. The particle aspect ratio is a quantification of the extend of deformation in the deposited particles. However, for the HVOF and plasma sprayed coatings processed at higher temperature conditions, the aspect ratio measurements were not made as the particles had melted and splats were formed. As the traverse speed was increased in cold spray from 50 mm/s to 200 mm/s, a slight increase in coating porosity and decrease in particle aspect ratio is observed. As the spray gun travels faster across the deposit, the time of which a local region is exposed to the heated supersonic jet stream decreases. This reduces the local heat accumulation, decreasing the achievable particle deformation and affect the

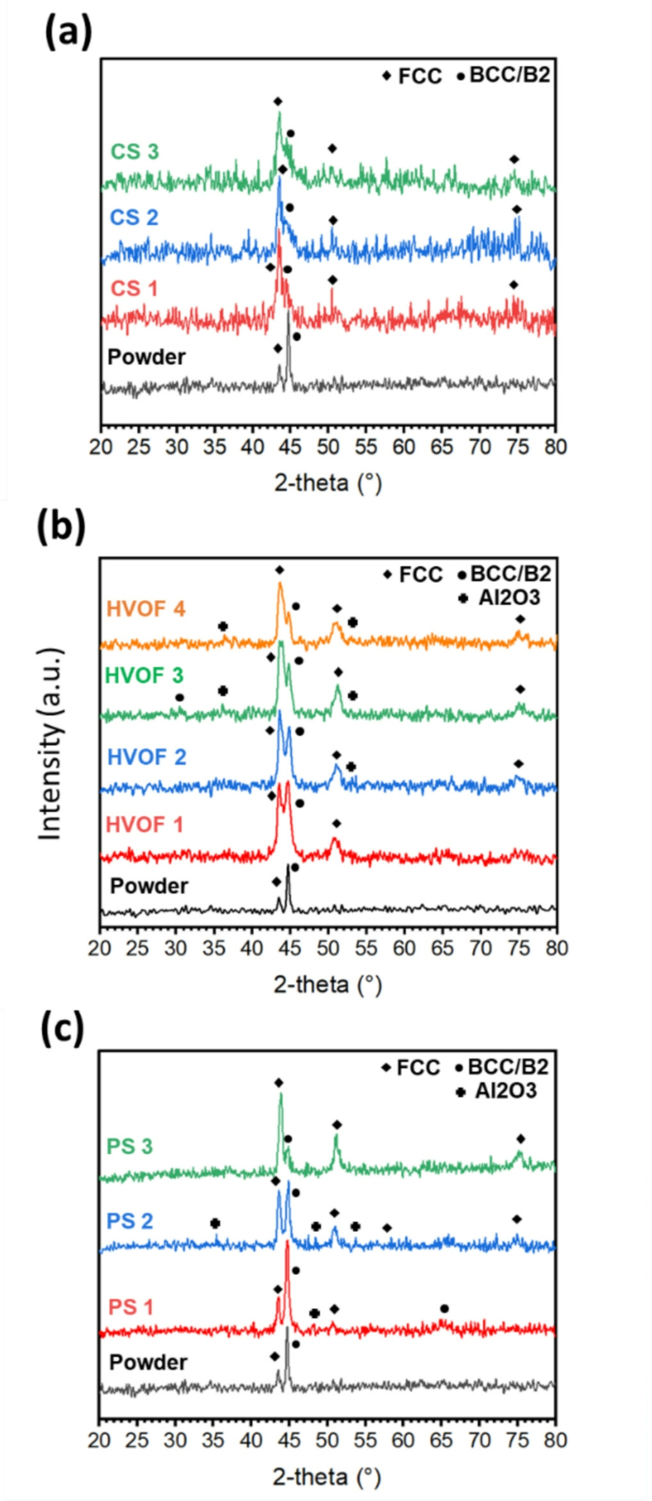

Fig. 2. XRD diffraction patterns of the feedstock powder and (a) cold sprayed coatings, (b) HVOF coatings, and (c) plasma sprayed coatings. All coatings show shift in the XRD patterns as compared to the powder, suggesting the occurrence of phase transformation after deposition.

bonding quality between particles, thereby resulting in higher porosity and lower particle aspect ratio. For the HVOF coatings, decreasing the SOD from 305 mm to 203 mm results in decrease in porosity. Increasing the effective processing temperature by increasing the flow of fuel also decreases the porosity of both the HVOF and plasma sprayed coatings. In PS 1, the measured particle aspect ratio is very low, and the measured porosity is much higher than the other two plasma sprayed coatings. This suggests that the sprayed particles have barely deformed, and the bonding achieved may have been poor.

3.3. *Phase analysis and microstructural characterization*

The XRD spectrums of the feedstock powder and the sprayed coatings are shown in Fig. 2. As compared with the pattern of the powder, which shows a high intensity bcc/B2 (110) peak with a weaker fcc (111) peak, all the coating samples show signs of phase transformation. From Fig. 2-a, the cold sprayed coatings all show a rise in intensity of the fcc peaks, and the (200) and (220) peaks that were not observable in the powder pattern now emerges.

While increasing the traverse speed did not lead to different XRD patterns in cold spray coatings, increasing the effective processing temperature in the HVOF and plasma sprayed coatings leads to the transition to a higher intensity fcc (111) peak with emerging fcc (200) and (220) peaks. The presence of the Al_2O_3 alumina is also detected, suggesting that the exposure to high thermal input in atmospheric environment may have led to oxidation.

In terms of the microstructure, the cold sprayed coatings were able to preserve the lamellar microstructure, as shown in Fig. 3. Micropores and thin gaps are found at particle interfaces, showing lack of metallurgical bonding. In Fig. 3-f, it can be observed how having high density of micropores in one spot can ultimately lead to the formation of interface gaps between particles. As shown in Table 3, increasing traverse speed from 50 to 200 mm/s leads to slight increase in porosity accompanied by lower degrees of particle deformation. For individual particles, the lamellar structure is significantly stretched and elongated along the direction of deformation. The sub-microscale lamellar structure also appears to be comparable to the feature size in the powder in Fig. 1-b.

In Fig. 4, the HVOF coatings show a significant difference in the microstructure as the processing conditions are changed. At a higher SOD with lower flow rates of kerosene and oxygen, near spherical particles with the lamellar structure can be observed (Fig. 4-a). Contrary, for the coatings processed at shorter SOD and higher fuel flow rates, the lamellar structure is no longer observable. Instead, the dark oxide layers and the molten particle splats form a new larger scale lamellar structure. Particle boundaries become undefinable as particles are melted into splats and mixed thoroughly in the coating.

The PS 1 coating clearly shows that the plasma jet did not attain sufficient temperature to homogeneously melt the feedstock powder. As shown in Fig. 5-a and b, many of the particles appear no difference than the starting feedstock powder. The quality of the particle bonding is questionable, and some particles appear to be simply trapped and locked between surrounding particles without clear signs of bonding at particle interfaces. In this case, most of the dark regions in the coatings are not oxides, but pores. When the flow rate of H_2 is increased, the processing temperature is sufficiently high to melt the powder particles into splats. Comparable to the trend observed in the HVOF coatings, the plasma sprayed coatings become more homogeneous with mixtures of oxides as the effective processing temperature increases.

3.4. *Elemental distribution*

To analyze the oxides present and the elemental distribution in the coatings, EDS cross-section elemental mapping was conducted. Figs. 6 to 8 show the EDS mappings of two coatings sprayed by each of the three processes. The distribution of the Al and O mapping shows that the dark oxides observed in the HVOF, and plasma sprayed coatings mainly corresponds to aluminum oxide (Al_2O_3). The measured elemental compositions obtained from EDS cross-section scanning from regions in Figs. 6–8 are listed in Table 4. The cold sprayed coatings show small increase in the oxygen content as compared to the feedstock powder, suggesting that oxidation is effectively mitigated by solid state deposition of particles even when employing a high gas temperature of 950 °C.

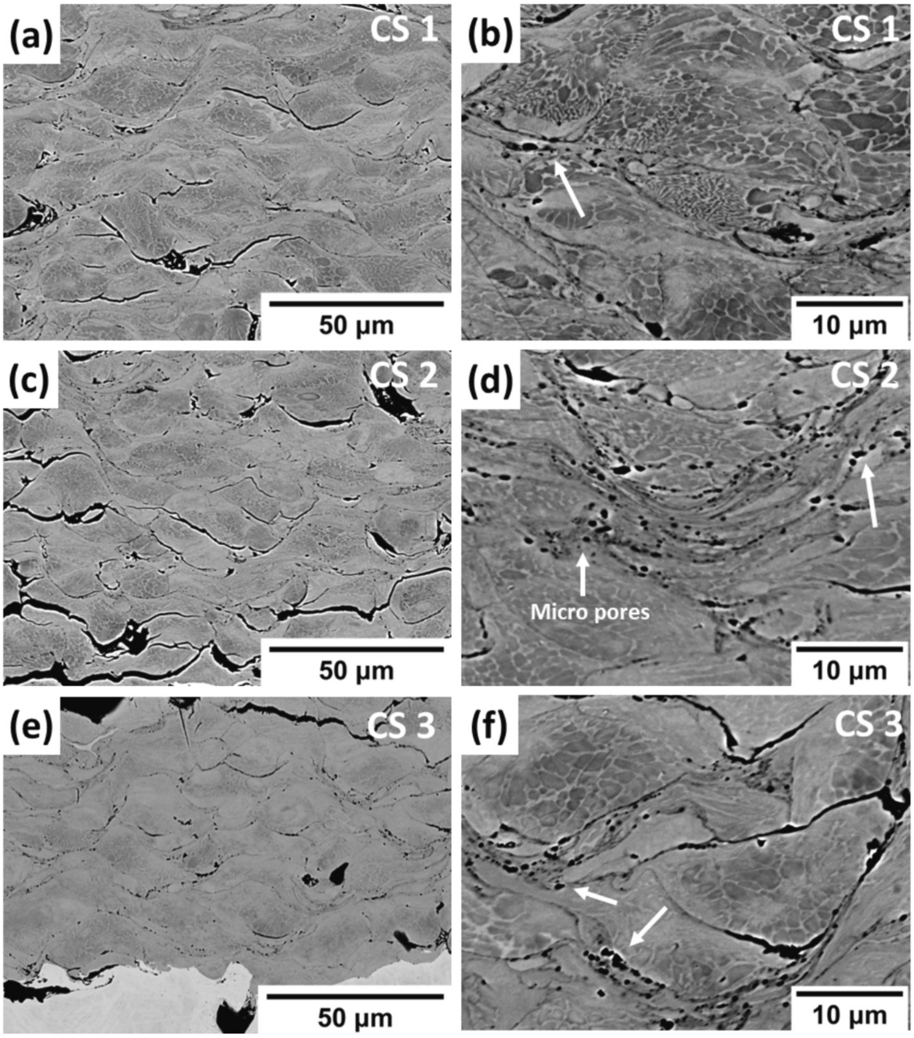

Fig. 3. SEM micrographs of the cold sprayed coating cross-sections of (a–b) CS 1, (c–d) CS 2, and (e–f) CS 3, micropores are highlighted by arrows. The lamellar structure from the feedstock powder is preserved.

However, higher traverse speed appears to have resulted in slight increase in oxidation of the coating. Due to limitations on the resolution obtainable in the EDS instrument, the lamellar structure could not be identified by the elemental mapping, and the observed oxygen distribution is rather homogeneous.

All coatings produced by HVOF are highly oxidized. The amount of oxide introduced increases with decrease of the SOD and increase of the fuel flow rate, with very high amount of oxygen up to 28.08 at.% in HVOF 4. Similar trend of increase in oxygen content is also observed in the plasma sprayed coatings, with lower extends of oxidation as compared to the HVOF coatings. Differences in the distribution of oxides can also be observed. For HVOF and plasma sprayed coatings produced with lower processing temperatures (larger SOD, lower fuel flow rate), the oxides are concentrated at particle interfaces (Figs. 7-a, 8-a), and the inner regions of the particles remain low of oxygen. In contrast, as particles are melted into splats at higher processing temperatures (Figs. 7-b, 8-b), the oxides are less concentrated and are mixed more homogeneously in the coating.

Due to limitations on the resolution obtainable from EDS, the submicroscale lamellar structure could not be clearly captured, therefore, EPMA was used to conduct WDS elemental mapping on the powder as well as the coating samples. Figs. 9 to 11 show the WDS elemental mappings of one coating sample from each of the three techniques, compared to the mapping of the powder shown in Fig. 1-c.

The mapping of CS 1 (Fig. 9) shows that the lamellar structure of the feedstock powder is well preserved in the coating, indicating that the cold spray process has effectively preserved the microstructure of the feedstock powder. A very fine layer of oxide exists at particle interfaces and micropores. The distribution of Co and Ni appears to be homogeneous in the coating. The mapping of HVOF 1 (Fig. 10) shows the presence of various oxides. While alumina remains to be the main oxide as suggested by EDS results, some Co and Ni oxides can also be found. The oxides are still highly concentrated at particle/splat interfaces. The inner regions of the particles/splats have much lower concentration of Al and very low concentration of oxygen. The lamellar structure from the powder can still be observed in unmelted particles (Fig. 10-a), and faintly outlined by the distribution of Al (Fig. 10-b). Fig. 11 shows the mapping of PS 3 that was deposited at a higher process temperature. Due to the extensive melting and mixing of the particle splats, the lamellar structure is no longer present. The oxides are less restricted to particle/splat interfaces, and small regions of Co and Ni oxides can be observed while Al remains to be the main oxide.

In both HVOF and plasma sprayed coatings, a clear segregation of Al can be observed. The formation of Al_2O_3 led to the diffusion of Al in inner particle regions to particle/splat interfaces, resulting in depletion of Al in oxide-free regions.

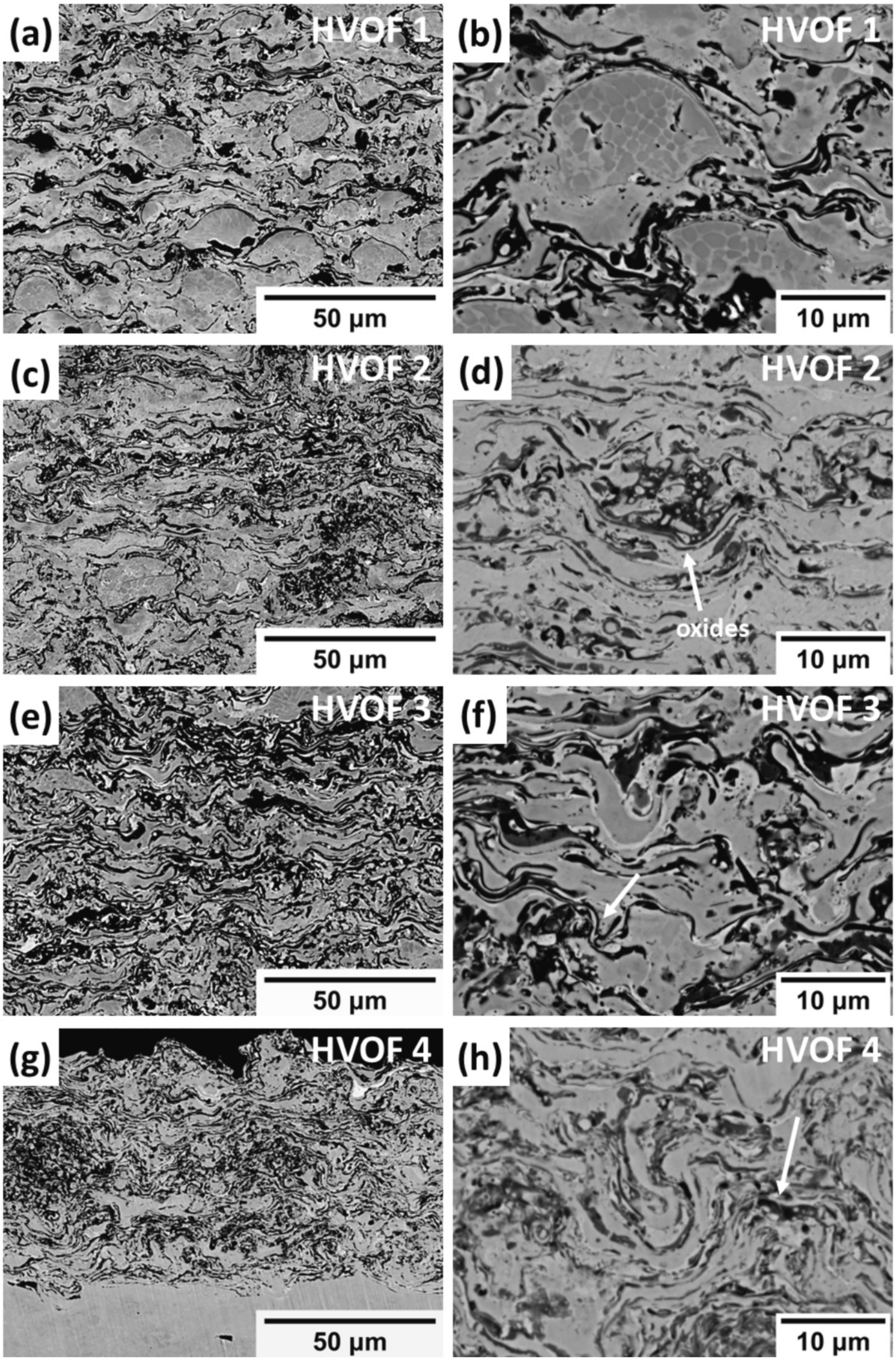

Fig. 4. SEM micrographs of the HVOF coating cross-sections of (a–b) HVOF 1, (c–d) HVOF 2, (e–f) HVOF 3, and (g–h) HVOF 4. Oxides are highlighted by white arrows. The layers of oxide and particle splats stack and mix to form a new lamellar structure.

3.5. Microhardness measurements

To evaluate the microhardness of the coatings, Vickers hardness indentation was conducted on both the polished coating top surfaces and cross-sections. Fig. 12 shows graph of Vickers microhardness versus oxygen content of the coatings, and Table 5 lists the microhardness values of the coatings with their oxygen content and porosity.

By evaluating the microhardness of the coatings with their oxygen contents, the coatings are grouped by the deposition methods. The cold sprayed coatings show high hardness in the range of 440 HV to 500 HV while maintaining low oxygen content below 4 %. Varying the traverse speed from 50 mm/s to 200 mm/s did not have significant impact on the microhardness. The HVOF coatings appear to show similar or even higher hardness as compared to the cold sprayed coatings, but with much higher oxygen content. Furthermore, a clear correlation can be established between the microhardness performance of the HVOF and plasma sprayed coatings with their oxygen content. The presence of oxide may have introduced oxide dispersion strengthening, enhancing the hardness of the coatings. The lamellar arrangement of the brittle oxides and splats (Fig. 4) may have also further enhanced coating hardness due to the ordered stacking (interface strengthening). Contrary to the cold spray and HVOF coatings, the hardness of the plasma sprayed coatings are much lower. Increasing the amount of oxygen content does also increase the hardness in the plasma spray coatings. Both the HVOF 1

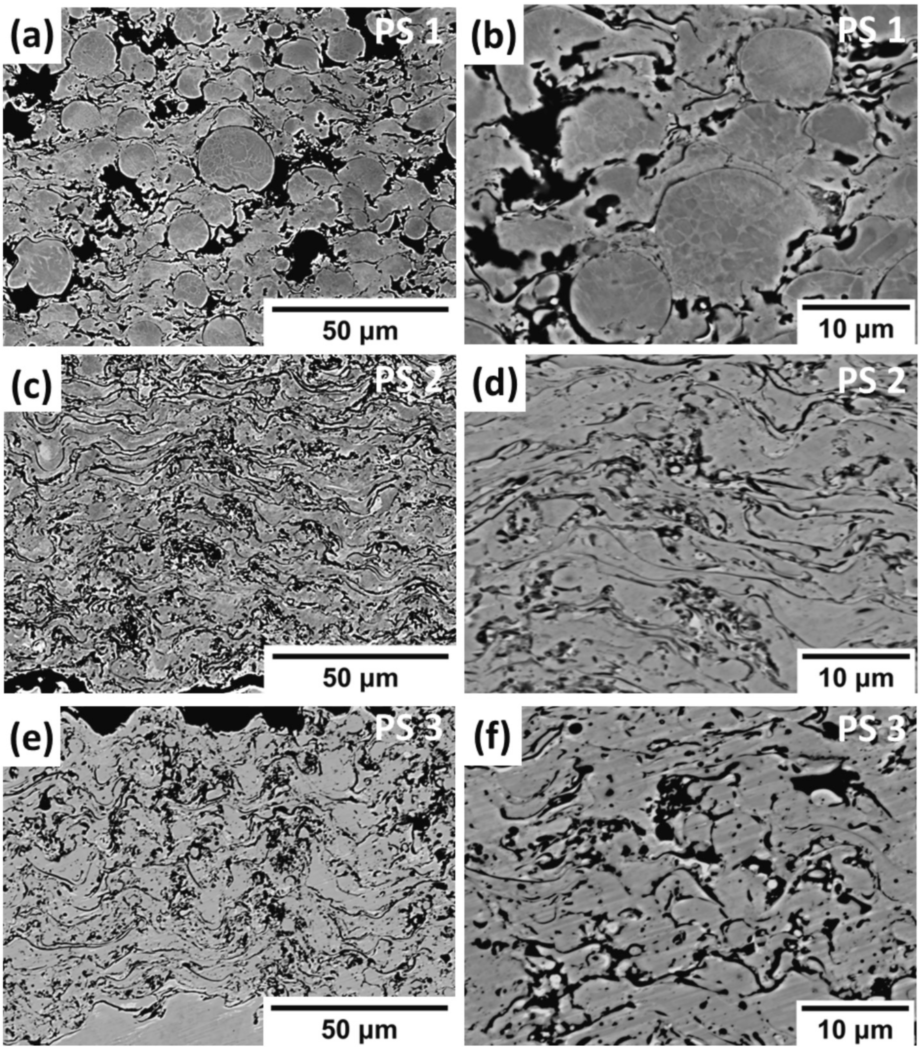

Fig. 5. SEM micrographs of the plasma sprayed coating cross-sections of (a–b) PS 1, (c–d) PS 2, and (e–f) PS 3. Insufficient processing temperature results in unmelted powder particles in (a–b).

and PS 1 coatings which show signs of incomplete particle melting due to insufficient processing temperature exhibit lower hardness, likely due to the weaker particle bonding as well as the higher porosity. Overall, the top surface hardness of the cold sprayed and HVOF coatings is higher than the cross-section hardness, which could be results of the shot peening effect and work hardening in the direction of layer buildup. The plasma sprayed coatings do not show evidence of this anisotropic behaviour. Furthermore, the density of interface pores and interparticle gaps are higher on coating cross-sections due to the direction of particle deformation. This is captured and reflected by the cross-section hardness measurements.

4. Discussion

4.1. Formation of oxides and phase transformations

As the XRD results pointed out, both the HVOF and plasma sprayed coatings show a clear sign of phase transformation where the relative intensity of the signal corresponding to the fcc peaks increases as the effective processing temperature increases (Fig. 2). By analysing the SEM micrographs (Figs. 4 and 5) and the elemental mappings (Figs. 7, 8, 10, and 11), clear signs of Al segregation in the coating are observed due to the formation of Al_2O_3. The amount of oxide formed increases as the effective processing temperature is increased, reducing the concentration of Al in the non-oxide regions. It has been well established in reported studies that in the AlCoCrFeNi system, Al acts as the stabilizer for the bcc/B2 phase and Ni acts as the stabilizer for the fcc phase [9,24]. When the Al is depleted in NiAl rich bcc/B2 regions, the bcc/B2 phase loses its stability, leading to transformation to the fcc phase and the breakdown of the original lamellar structure.

On the other hand, the phase transformation observed in the cold sprayed coatings occurs from a different mechanism. Although the XRD results (Fig. 2) suggest that the dominant phase present has shifted from bcc/B2 to fcc, we see that the microstructure as well as the elemental mapping of the cold sprayed coatings (Figs. 3, 6, and 9) are very similar to the feedstock powder (Fig. 1). No clear sign of elemental segregation or interdiffusion was observed. Pan et al. [8] reported that when gas atomized $AlCoCrFeNi_{2.1}$ powder is sintered at 800 °C and 900 °C at 30 MPa pressure for 5 min, similar phase transformation was observed in the XRD pattern. The fcc peak intensity overcomes the bcc peaks while no clear changes to the lamellar eutectic microstructures were visible. At higher sintering temperatures, they reported that the lamellar structure gradually disappeared as the fcc phase grows and form massive eutectic structures [8]. Charkhchian et al. [25] studied the microstructure of as-casted $AlCoCrFeNi_{2.1}$. They observed larger fcc phases taking the form of dendrites with small inter-dendritic regions occupied by the lamellar eutectic structure. The XRD pattern of the as-casted $AlCoCrFeNi_{2.1}$ also shows a much stronger fcc pattern compared to the bcc pattern. Under

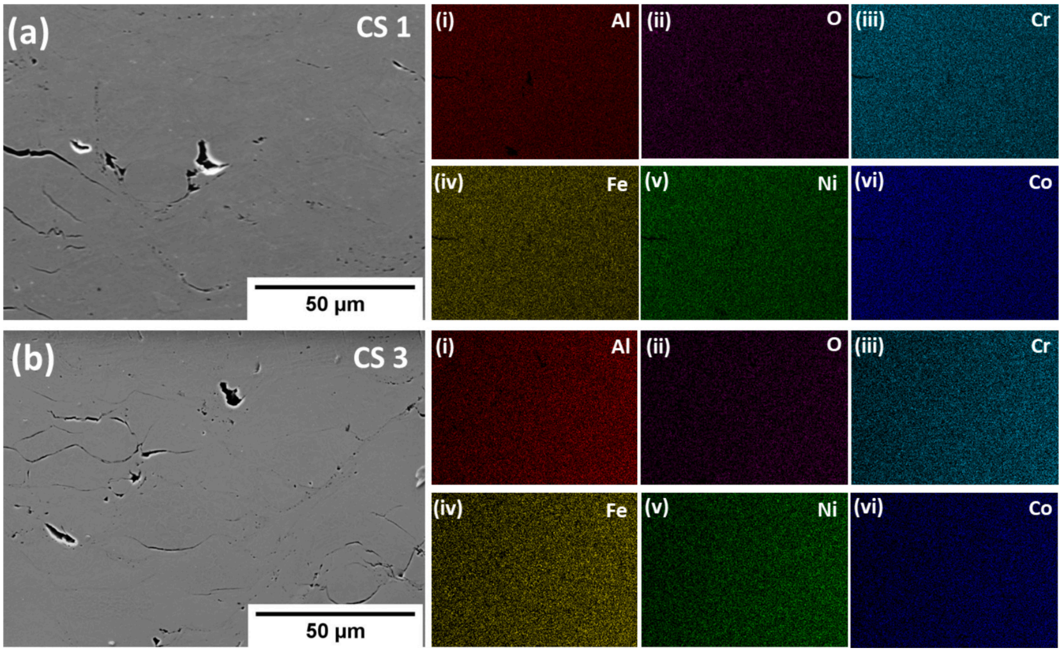

Fig. 6. EDS cross-section elemental mapping of (a) CS1 and (b) CS 3, with the elemental distributions listed in (i–vi). No clear signs of elemental segregation or concentration of oxides are observed.

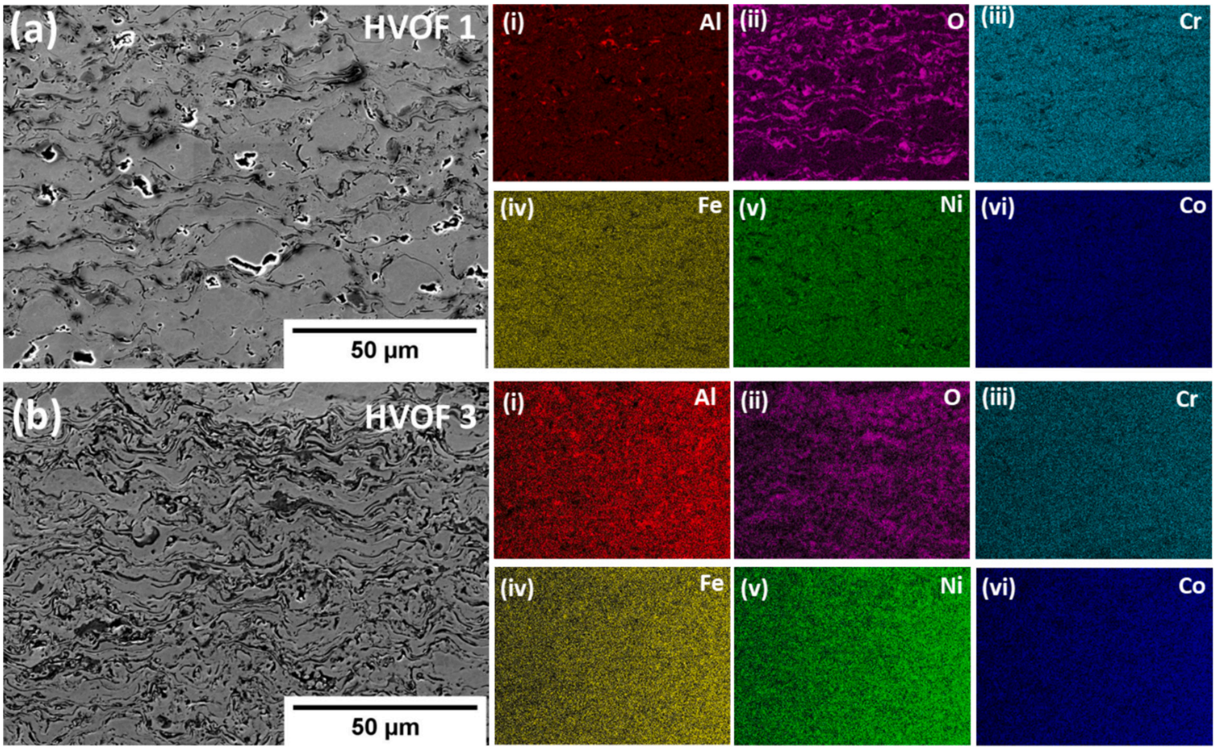

Fig. 7. EDS cross-section elemental mapping of (a) HVOF 1 showing oxides concentrated at particle interfaces and (b) HVOF 3 showing oxides mixed more homogenously in coating due to particles melting and splats formation and mixing. The elemental distributions are listed in (i–vi), and the distribution of Al_2O_3 is clearly captured in (i–ii).

slower cooling rates in processes such as casting, the material can attain uniform equilibrium solidification and reach its most stable phase and microstructure in the ambient conditions of the cooling environment. The fine lamellar structure and the NiAl rich bcc/B2 phase may be the results of non-equilibrium solidification due to the rapid cooling in the gas atomization process. During cold spray, the exposure to the high temperature jet stream and the instantaneous localized adiabatic heating from particle collisions may have supplied enough energy to overcome the barriers for phase transformations. This leads to a non-diffusion phase transformation where the metastable bcc/B2 crystal structure rearranges to form the fcc phase. Compared with MCrAlY coatings, Richer et al. [21] reported that cold sprayed gas atomized

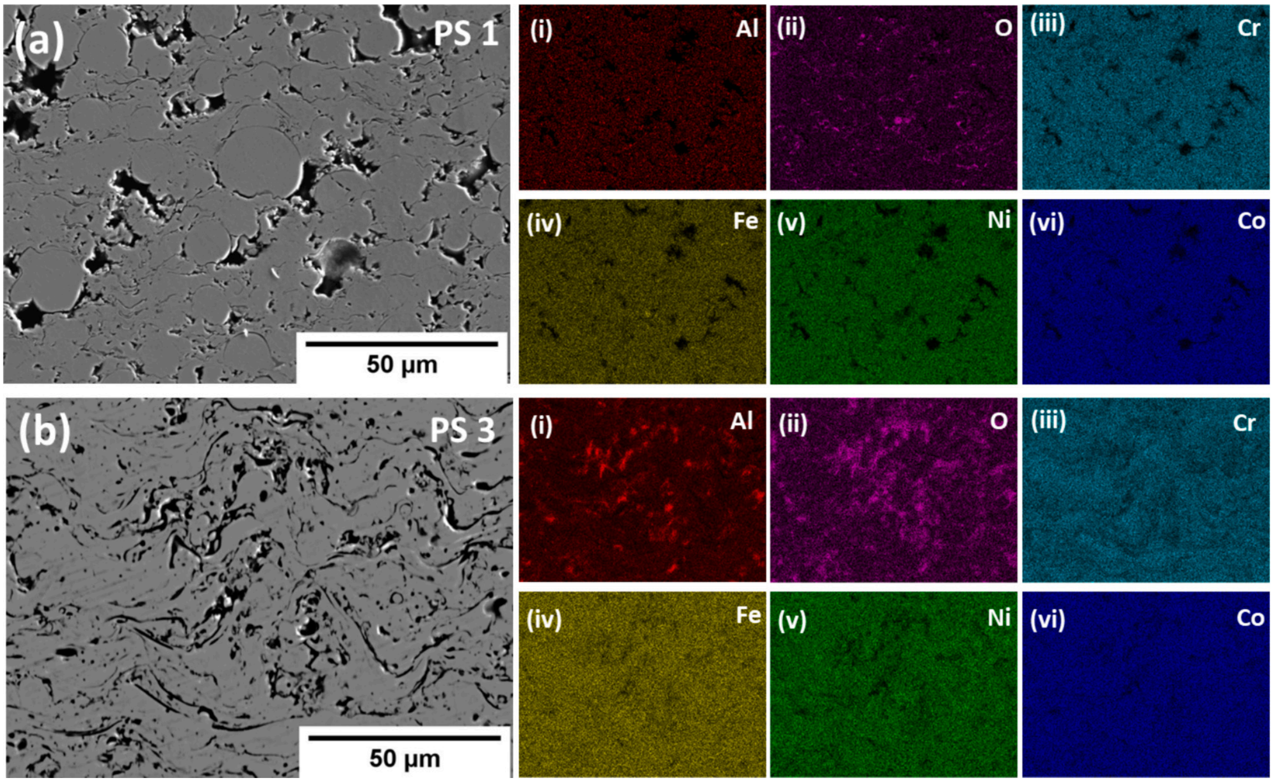

Fig. 8. EDS cross-section elemental mapping of (a) PS 1 showing oxides concentrated at particle interfaces and (b) PS 3 showing oxides mixed more homogenously in coating due to good mixing of particle splats. The elemental distributions are listed in (i–vi), and the distribution of Al_2O_3 is clearly captured in (i–ii).

Table 4
Elemental composition of the coatings obtained from EDS cross-sectional scan.

Element (at.%)	Powder	CS 1	CS 2	CS 3	HVOF 1	HVOF 2	HVOF 3	HVOF 4	PS 1	PS 2	PS 3
O	1.23	2.32	3.08	3.87	13.42	19.12	24.36	28.08	6.11	9.10	13.44
Al	15.71	16.19	16.31	16.45	14.00	11.61	13.34	12.65	15.55	14.90	12.58
Cr	16.60	16.91	16.72	16.15	14.07	13.30	12.09	12.36	15.97	14.70	11.76
Fe	15.81	16.17	15.91	15.75	14.34	15.60	12.51	12.41	15.65	15.25	14.42
Co	16.30	16.04	15.83	15.60	14.54	13.56	12.56	11.72	15.38	15.18	15.52
Ni	34.35	32.35	32.16	32.18	29.64	26.80	25.14	22.77	31.33	30.89	32.27

CoNiCrAlY, a common MCrAlY material used in high temperature protective coating applications [20–22], showed a change in the microstructure where the AlNi precipitate was dissipated into the CoCrNi rich fcc matrix, leading to the disappearance of the bcc/B2 peaks in the XRD pattern. Both the cold sprayed $AlCoCrFeNi_{2.1}$ and CoNiCrAlY show an fcc dominant microstructure without introducing significant oxidation in the coating.

4.2. Microhardness and strengthening mechanisms

As shown in Fig. 12, the microhardness performance of the coatings can be grouped by their processing techniques. When the powder particles are sprayed towards the substrate, there exists a work hardening process as the particles impact the substrate or the deposited particles. This work hardening mechanism leads to anisotropic mechanical properties where the material is strengthened along the direction of the applied load, which is perpendicular to the substrate in the cases of the three processing techniques discussed in this study. This contributed to the anisotropic behaviour in the microhardness where the top surface hardness of the coating is greater than the cross-section hardness. The degree of strengthening by work hardening is highly dependent on the applied load and the temperature. Both cold spray and HVOF processes create supersonic jet velocities [12,17,19], which drastically increase the impact velocity of the powder particles. In cold spray, severe plastic deformation from particle impact is the key to achieve successful bonding, hence the effect of work hardening is significant. The work hardening ability would be weaker in the HVOF coatings due to the high temperature jet stream. In contrast, the jet stream in plasma spray is typically subsonic, resulting in lower particle impact velocities. This is also observable from the SEM micrographs in Figs. 3–5 and the measured particle aspect ratios. The PS 1 coating show very low extends of deformation, followed by HVOF 1 and finally the cold sprayed coatings. For the HVOF and plasma spray processes where the contribution of thermal energy is greater, the work hardening of the material is drastically decreased. Furthermore, the sub-microscale lamellar structure preserved in the cold sprayed coatings can also enhance the mechanical performance of the coating. This leads to the overall differences in microhardness of coatings produced by the three techniques.

The high concentration of the brittle Al_2O_3 oxides does effectively increase the hardness of the HVOF. The oxide dispersion strengthening effect as well as the lamellar arrangement of the oxide layers significantly improve the hardness of the coatings. Similar strengthening effect is also observed in the plasma sprayed coatings which has lower concentration of oxides. However, the presence of oxides may not be beneficial for all applications and is extremely difficult to remove. Depending on the designed application, it can be a structural

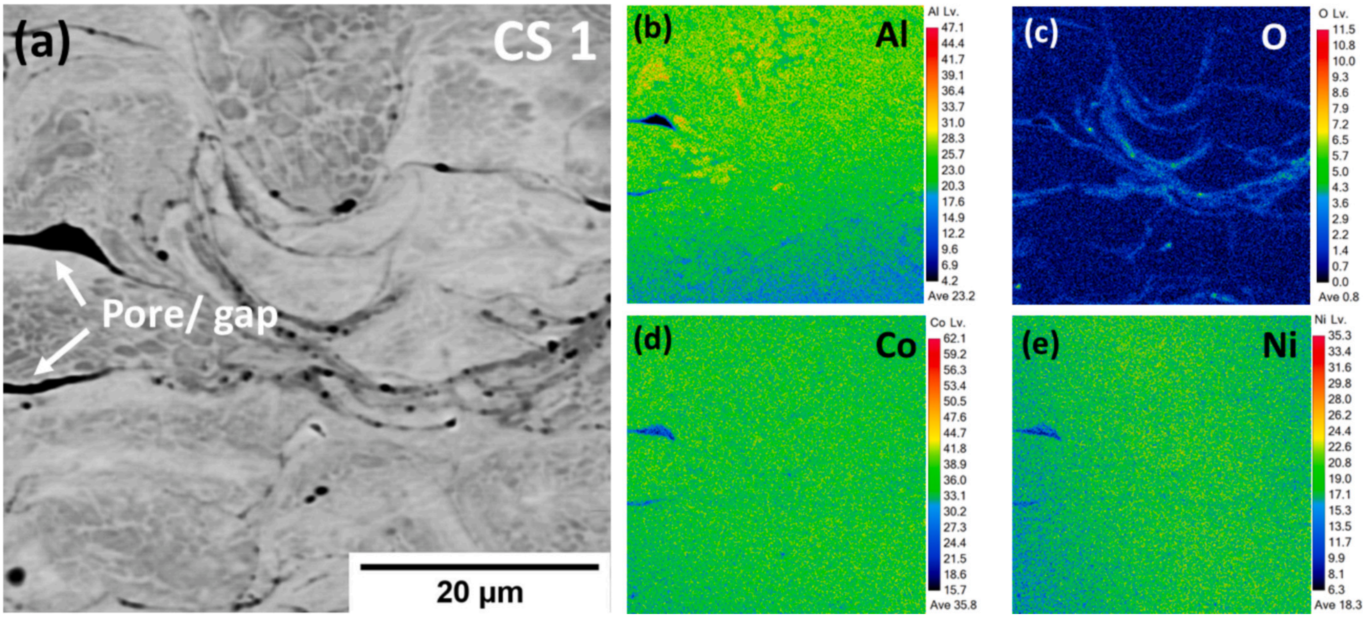

Fig. 9. WDS elemental mapping of the CS 1 coating cross-section, (a) the BSE micrograph, (b–d) elemental mapping of Al, O, Co, and Ni, respectively. The lamellar structure with the NiAl rich regions is captured in (b). Thin layers of oxides concentrated at particle interfaces.

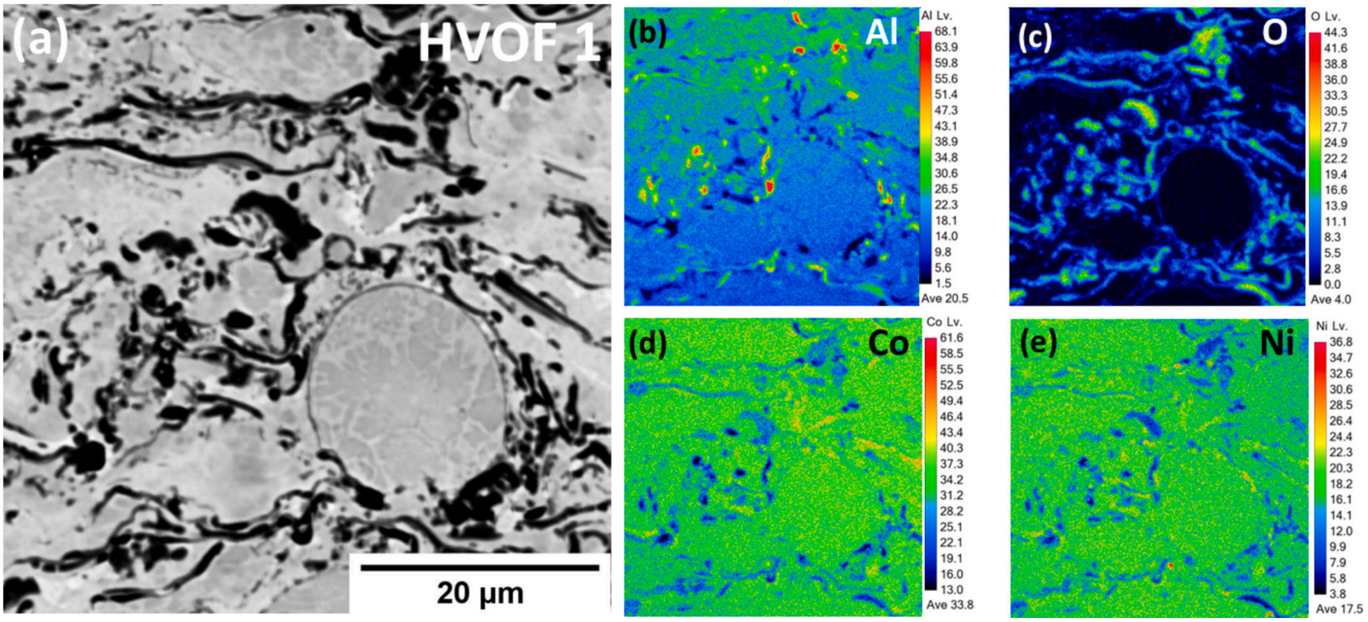

Fig. 10. WDS elemental mapping of the HVOF 1 coating cross-section, (a) the BSE micrograph, (b–d) elemental mapping of Al, O, Co, and Ni, respectively. Clear signs of segregation of Al are observed in (b), the oxides are more concentrated at particle/splat interfaces.

improvement or an undesired contamination. While oxidation embrittlement can lead to significant loss of ductility in the coating that can be detrimental to its service life, the difference in the distribution of oxides (layered vs. homogeneous mixtures) can also lead to different oxidation resistant performances. Would the preserved lamellar structure in the oxide free cold sprayed coatings lead to better oxidation resistance? The performance and behaviour of these coating under long term heating is an interesting direction of future work that can further evaluate the potential in AlCoCrFeNi$_{2.1}$ to be proposed as an alternative to the MCrAlY materials in high temperature protective coating applications.

5. Summary

In this study, we have fabricated AlCoCrFeNi$_{2.1}$ EHEA coatings using the cold spray, HVOF, and plasma spray techniques. The following conclusions have been drawn:

1) **Powder deposition and coating formation:** Overall, all the coatings show relatively high density and lower porosity. Decreasing the traverse speed of nozzle from 200 mm/s to 50 mm/s reduces the porosity in the cold sprayed coatings by suppressing micropores and gaps at particle-particle interfaces. Increasing the effective processing temperature by reducing the SOD from 203 mm to 305 mm or

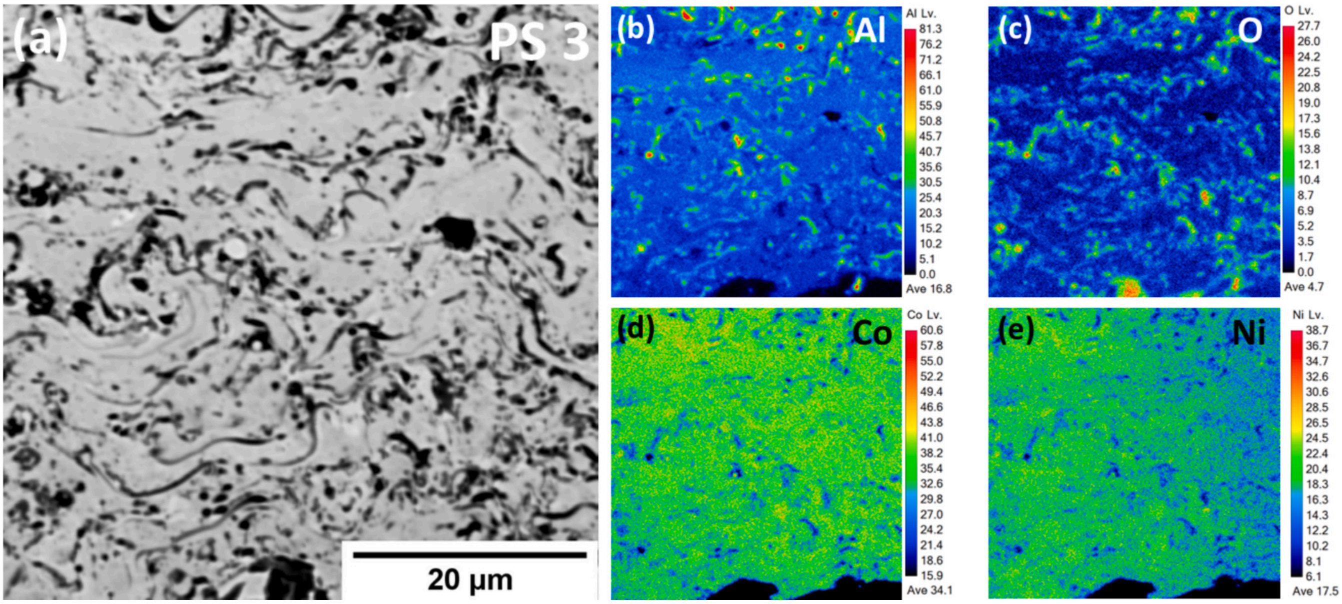

Fig. 11. WDS elemental mapping of the PS 3 coating cross-section, (a) the BSE micrograph, (b–d) elemental mapping of Al, O, Co, and Ni, respectively. Clear signs of segregation of Al are observed in (b), oxides are mixed more homogeneously in the coating and not restricted to splat interfaces.

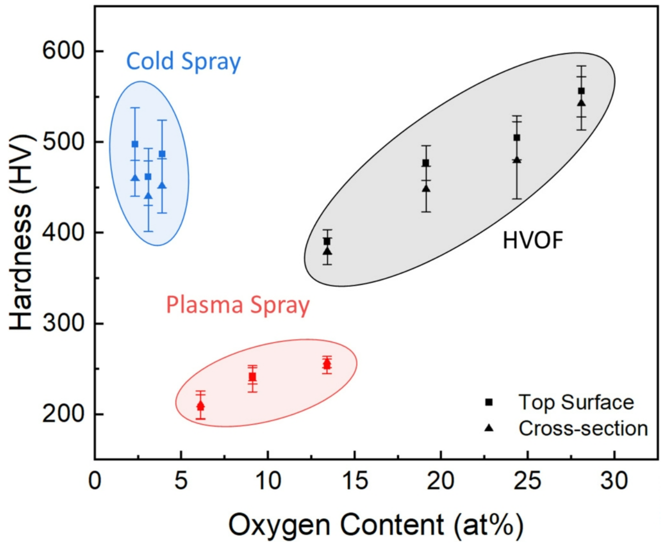

Fig. 12. Graph of Vickers microhardness versus oxygen content. Hardness was evaluated on both top surface and cross-section of the coatings. The obtained hardness values of the three deposition techniques are compared.

Table 5
Microhardness measurements of the coatings listed with their oxygen content and porosity.

Coatings	Top surface hardness (HV)	Cross-section hardness (HV)	Oxygen content (at. %)	Porosity (%)
CS 1	498.2 ± 39.9	460.3 ± 19.7	2.32	1.52 ± 0.89
CS 2	461.9 ± 31.3	440.5 ± 39.0	3.08	1.9 ± 0.90
CS 3	487.1 ± 37.3	452.0 ± 29.7	3.87	2.12 ± 0.37
HVOF 1	390.2 ± 13.4	379.9 ± 14.6	13.42	0.94 ± 0.16
HVOF 2	477.3 ± 19.1	448.3 ± 25.4	19.12	0.21 ± 0.04
HVOF 3	505.1 ± 24.4	480.2 ± 42.8	24.36	0.20 ± 0.03
HVOF 4	556.3 ± 28.1	543.1 ± 29.3	28.08	0.09 ± 0.04
PS 1	207.9 ± 6.1	210.7 ± 15.3	6.11	1.64 ± 0.40
PS 2	242.6 ± 9.1	239.2.4 ± 14.5	9.10	0.17 ± 0.07
PS 3	257.7 ± 13.4	252.9 ± 7.9	13.44	0.84 ± 0.18

increasing the fuel gas increases the oxygen content in both HVOF and plasma sprayed coatings.

2) **Microstructure and phases:** Cold spray promotes the rearrangement of the lamellar microstructure and the phase transformation from the bcc/B2 phase to the fcc phase. The high processing temperatures in the HVOF and plasma spray promote the development of Al_2O_3 and small amounts of other oxides. The formation of Al_2O_3 segregates the Al from NiAl-rich bcc/B2 regions, leading to a transformation to the FeCoCr-rich fcc phase. By melting the powder particles into splats, the sub-microscale lamellar structure is lost and, instead, replaced by a microscale lamellar structure arranged by the stacking of the oxide strips alternated with the particle splats.
3) **Hardness:** The cold sprayed coatings exhibit microhardness in the range of 441 HV and 498 HV due to significant work hardening while maintaining low oxygen content below 4 at.%. The hardness of HVOF coatings show a strong correlation with the oxygen content present, and a high hardness of 556.3 HV with 28.1 at.% oxygen in HVOF 4 was observed. The plasma sprayed coatings show lower oxygen content as compared to the HVOF coatings but also exhibit similar oxide dispersion strengthening mechanism with lower microhardness in the range of 208–258 HV.
4) **Comparison:** This study demonstrates that cold spray is a promising method to produce AlCoCrFeNi2.1 EHEA coatings with high hardness while maintaining low porosity and oxidation. For future work, it is interesting to compare the performance of the AlCoCrFeNi2.1 EHEA coatings with MCrAlY materials in high temperature experiments to further investigate the potential of finding alternatives for MCrAlY materials in high temperature protective coating applications.

CRediT authorship contribution statement

Jingjie Wei: Writing – original draft, Methodology, Investigation, Formal analysis, Data curation, Conceptualization. **Cristian Cojocaru:** Writing – review & editing, Resources, Methodology, Conceptualization. **Maniya Aghasibeig:** Writing – review & editing, Methodology, Conceptualization. **Chenwei Shao:** Writing – review & editing, Validation, Investigation, Formal analysis. **Zehua Li:** Software, Methodology. **Jiahui Zhang:** Software, Methodology. **Eric Irissou:** Supervision, Writing – review & editing. **Yu Zou:** Writing – review & editing, Supervision, Resources, Project administration, Funding acquisition.

Declaration of competing interest

The authors declare the following financial interests/personal relationships which may be considered as potential competing interests: Yu Zou reports financial support was provided by National Research Council Canada. If there are other authors, they declare that they have no known competing financial interests or personal relationships that could have appeared to influence the work reported in this paper.

Acknowledgements

The authors acknowledge NRC-CSTIP grant #AM-127-1 and NRC Advanced Manufacturing Program (AMP) funding support. The authors thank the members of the Laboratory for Extreme Mechanics & Additive Manufacturing (LEMAM) for their experimental support and helpful suggestions, Dr. Yanan Liu (Department of Earth Sciences, University of Toronto) for her experimental support and technical expertise.

Data availability

Data will be made available on request.

References

[1] E.P. George, D. Raabe, R.O. Ritchie, High-entropy alloys, Nature Reviews Materials 2019 4:8 4 (2019) 515–534. doi:https://doi.org/10.1038/s41578-019-0121-4.

[2] E.P. George, W.A. Curtin, C.C. Tasan, High entropy alloys: a focused review of mechanical properties and deformation mechanisms, Acta Mater. 188 (2020) 435–474, https://doi.org/10.1016/J.ACTAMAT.2019.12.015.

[3] D.B. Miracle, O.N. Senkov, A critical review of high entropy alloys and related concepts, Acta Mater. 122 (2017) 448–511, https://doi.org/10.1016/J.ACTAMAT.2016.08.081.

[4] M.H. Tsai, J.W. Yeh, High-entropy alloys: a critical review, Mater Res Lett 2 (2014) 107–123, https://doi.org/10.1080/21663831.2014.912690.

[5] K. Cui, Y. Zhang, High-entropy alloy films, Coatings 2023, Vol. 13, Page 635 13 (2023) 635. doi:https://doi.org/10.3390/COATINGS13030635.

[6] S.K. Dewangan, A. Mangish, S. Kumar, A. Sharma, B. Ahn, V. Kumar, A review on high-temperature applicability: a milestone for high entropy alloys, Engineering Science and Technology, an International Journal 35 (2022) 101211, https://doi.org/10.1016/J.JESTCH.2022.101211.

[7] Y.F. Ye, Q. Wang, J. Lu, C.T. Liu, Y. Yang, High-entropy alloy: challenges and prospects, Mater. Today 19 (2016) 349–362, https://doi.org/10.1016/J.MATTOD.2015.11.026.

[8] L. Wang, F. Zhang, H. Ma, S. He, F. Yin, Microstructure evolution and mechanical properties of plasma sprayed AlCoCrFeNi2.1 eutectic high-entropy alloy coatings, Surf. Coat. Technol. 471 (2023) 129924, https://doi.org/10.1016/J.SURFCOAT.2023.129924.

[9] W. Pan, P. Fu, Z. Li, H. Chen, Q. Tang, P. Dai, C. Liu, L. Lin, Microstructure and mechanical properties of AlCoCrFeNi2.1 eutectic high-entropy alloy synthesized by spark plasma sintering of gas-atomized powder, Intermetallics (Barking) 144 (2022) 107523, https://doi.org/10.1016/J.INTERMET.2022.107523.

[10] T. Xiong, S. Zheng, J. Pang, X. Ma, High-strength and high-ductility AlCoCrFeNi2.1 eutectic high-entropy alloy achieved via precipitation strengthening in a heterogeneous structure, Scr. Mater. 186 (2020) 336–340, https://doi.org/10.1016/J.SCRIPTAMAT.2020.04.035.

[11] H. Chen, L. Lang, X. Shang, S.S. Dash, Y. He, G. King, Y. Zou, Anisotropic co-deformation behavior of nanolamellar structures in additively manufactured eutectic high entropy alloys, Acta Mater. 271 (2024) 119885, https://doi.org/10.1016/J.ACTAMAT.2024.119885.

[12] Y. Zou, Cold spray additive manufacturing: microstructure evolution and bonding features, Acc Mater Res 2 (2021) 1071–1081, https://doi.org/10.1021/accountsmr.1c00138.

[13] A. Papyrin, V. Kosarev, S. Klinkov, A. Alkimov, V. Fomin, Current status of the cold spray process, Cold Spray Technology (2007) 248–323, https://doi.org/10.1016/B978-008045155-8/50005-3.

[14] J. Huang, W. Sun, X. Chu, H. Lan, Y. Xie, D. Ye, R. Huang, Effect of high temperature exposure on microstructure, mechanical and tribological properties of cold sprayed NiCoCrAlTaY coatings, Surf. Coat. Technol. 462 (2023) 129466, https://doi.org/10.1016/J.SURFCOAT.2023.129466.

[15] J. Wei, M. Aghasibeig, T. Lyu, Z. Liu, H. Chen, E. Irissou, Y. Zou, Cold spray deposition and microstructure characterization of CuNi, CuSn, and CuNiSiCr coatings, Surf Coat Technol 480 (2024) 130621, https://doi.org/10.1016/J.SURFCOAT.2024.130621.

[16] J. Wei, Y. He, P. Vo, Y. Zou, Cold Spray in Practical and Potential Applications, Solid-state Metal Additive Manufacturing: Physics, Processes, Mechanical Properties, and Applications, 2024, pp. 101–132, https://doi.org/10.1002/9783527839353.CH5.

[17] J.D. Majumdar, Thermal and cold spraying technology in manufacturing, in: Handbook of Manufacturing Engineering and Technology, Springer London, 2013: pp. 1–37. doi:https://doi.org/10.1007/978-1-4471-4976-7_31-2.

[18] H. Assadi, F. Gärtner, T. Stoltenhoff, H. Kreye, Bonding mechanism in cold gas spraying, Acta Mater. 51 (2003) 4379–4394, https://doi.org/10.1016/S1359-6454(03)00274-X.

[19] D. Qadir, R. Sharif, R. Nasir, A. Awad, H.A. Mannan, A review on coatings through thermal spraying, Chemical Papers 2023 78:1 78 (2023) 71–91. doi:https://doi.org/10.1007/S11696-023-03089-4.

[20] H. Luo, X. Li, C. Pan, P. He, K. Zeng, K. Hu, H. Li, C. Yang, Microstructure and oxidation resistance of CoNiCrAlY coating manufactured by laser powder bed fusion, Surf. Coat. Technol. 427 (2021) 127846, https://doi.org/10.1016/J.SURFCOAT.2021.127846.

[21] P. Richer, A. Zúñiga, M. Yandouzi, B. Jodoin, CoNiCrAlY microstructural changes induced during cold gas dynamic spraying, Surf. Coat. Technol. 203 (2008) 364–371, https://doi.org/10.1016/J.SURFCOAT.2008.09.014.

[22] W.R. Chen, E. Irissou, X. Wu, J.G. Legoux, B.R. Marple, The oxidation behavior of TBC with cold spray CoNiCrAlY bond coat, J. Therm. Spray Technol. 20 (2011) 132–138, https://doi.org/10.1007/S11666-010-9601-1.

[23] V. Katranidis, S. Gu, B. Allcock, S. Kamnis, Experimental study of high velocity oxy-fuel sprayed WC-17Co coatings applied on complex geometries, Part A: influence of kinematic spray parameters on thickness, porosity, residual stresses and microhardness, Surf Coat Technol 311 (2017) 206–215, https://doi.org/10.1016/J.SURFCOAT.2017.01.015.

[24] W.R. Wang, W.L. Wang, S.C. Wang, Y.C. Tsai, C.H. Lai, J.W. Yeh, Effects of Al addition on the microstructure and mechanical property of AlxCoCrFeNi high-entropy alloys, Intermetallics (Barking) 26 (2012) 44–51, https://doi.org/10.1016/J.INTERMET.2012.03.005.

[25] J. Charkhchian, A. Zarei-Hanzaki, A. Moshiri, H.R. Abedi, J. Shen, J.P. Oliveira, K. Chadha, C. Aranas, On the short-time thermal phase-stability of as-cast AlCoCrFeNi2.1 eutectic high entropy alloy, J. Mater. Res. Technol. 20 (2022) 551–560, https://doi.org/10.1016/J.JMRT.2022.07.058.